




ARTICLE

<https://doi.org/10.1038/s42005-019-0212-y>

OPEN

Demonstration of the key substrate-dependent charge transfer mechanisms between monolayer MoS₂ and molecular dopants

Soohyung Park ^{1,2,3}, Thorsten Schultz ^{1,2}, Xiaomin Xu¹, Berthold Wegner¹, Areej Aljarb⁴, Ali Han⁴, Lain-Jong Li^{4,5}, Vincent C. Tung^{4,6}, Patrick Amsalem¹ & Norbert Koch ^{1,2}

Tuning the Fermi level (E_F) in two-dimensional transition metal dichalcogenide (TMDC) semiconductors is crucial for optimizing their application in (opto-)electronic devices. Doping by molecular electron acceptors and donors has been suggested as a promising method to achieve E_F -adjustment. Here, we demonstrate that the charge transfer (CT) mechanism between TMDC and molecular dopant depends critically on the electrical nature of the substrate as well as its electronic coupling with the TMDC. Using angle-resolved ultraviolet and X-ray photoelectron spectroscopy, we reveal three fundamentally different, substrate-dependent CT mechanisms between the molecular electron acceptor 1,3,4,5,7,8-hexafluoro-tetracyano-naphthoquinodimethane (F_6 TCNNQ) and a MoS₂ monolayer. Our results demonstrate that any substrate that acts as charge reservoir for dopant molecules can prohibit factual doping of a TMDC monolayer. On the other hand, the three different CT mechanisms can be exploited for the design of advanced heterostructures, exhibiting tailored electronic properties in (opto-)electronic devices based on two-dimensional semiconductors.

¹Humboldt-Universität zu Berlin, Institut für Physik & IRIS Adlershof, Brook-Taylor Straße 6, 12489 Berlin, Germany. ²Helmholtz-Zentrum für Materialien und Energie GmbH, Bereich Solarenergieforschung, Albert-Einstein-Straße 15, 12489 Berlin, Germany. ³Advanced Analysis Center, Korea Institute of Science and Technology (KIST), Seoul 02792, South Korea. ⁴Physical Sciences and Engineering, King Abdullah University of Science and Technology, Thuwal 23955-6900, Saudi Arabia. ⁵School of Materials Science and Engineering, The University of New South Wales, Sydney, NSW 2052, Australia. ⁶Molecular Foundry, Lawrence Berkeley National Lab, Berkeley, CA 94720, USA. Correspondence and requests for materials should be addressed to N.K. (email: norbert.koch@physik.hu-berlin.de)

Two-dimensional transition metal dichalcogenides (2D TMDCs) are promising next-generation semiconductor materials, owing to their superior electronic properties that originate from their low dimensionality and high symmetry^{1–3}. For practical 2D TMDC-based electronic devices, e.g., thin-film transistors (TFTs)^{4,5}, chemical sensors^{6–8}, photodetectors^{9,10}, and photovoltaic cells^{11–14}, one of the key challenges is controlling the doping level, and thus the Fermi level (E_F) position, of the 2D TMDC semiconductors without breaking their low dimensionality and high symmetry, so that the desired electrical properties are retained.

Various methods have been proposed for tuning E_F within the band gap of TMDCs, including substitution with dopant atoms¹⁵, stacking with other 2D materials¹⁶, exposure to gases^{6–8,17}, adsorption of alkali metals^{18,19}, and adsorption of organic molecules^{20–26}. In accordance with this approach, deposition of molecular electron acceptors or donors on TMDCs has been suggested as a very effective strategy for controlling the E_F position via doping, and accordingly high-performance TFTs were realized^{22,24,26}. However, the extent to which the changes in electrical TFT characteristics were indeed due to electron transfer between the dopant molecules and the monolayer TMDC (ML-TMDC) was not unambiguously demonstrated, and mostly changes of photoluminescence intensity of excitons versus trions were interpreted as signature of charge transfer (CT). A fundamental understanding of the CT mechanisms occurring at the interface between dopant molecules and ML-TMDCs as well as direct evidence of E_F position tuning, e.g., as typically achieved by photoelectron spectroscopy, are lacking, mostly because conductive substrates for the ML-TMDC were employed. For instance, Katoch et al.²⁷ investigated n-type doping of WS₂ by potassium atom deposition. However, degenerately doped, highly conductive TiO₂ was used as substrate, from which the ML-TMDC was separated only via an ultrathin boron nitride layer, and the role of the underlying metal oxide substrate remains elusive. Regardless, renormalization of the WS₂ band gap and spin-orbit splitting due to many-body effects was demonstrated.

Understanding the electronic properties of interfaces in devices such as those present in 2D TMDC-based devices is crucial for performance optimization. For instance, the TMDC/insulator interface determines the electronic properties of the active layer when a bias is applied to the gate in a TFT, while TMDC/metal interfaces serve as the electrical contacts between the semiconductor and the drain or source electrodes. In this context, it was demonstrated that the substrate dielectric properties significantly affect the electronic structure of ML-TMDC monolayers, such as band gap renormalization^{27,28}, and the TMDC–substrate interaction influences the exciton and trion binding energies (BEs)^{28,29}. Also of importance for devices is minimizing the Schottky barrier height between a metal contact and the TMDC, as pronounced Fermi level pinning seems to limit the range of tunability, as revealed via thermionic emission studies by Kim et al.³⁰. Here, the electronic coupling and chemical interaction between the TMDC and metals play vital roles. These findings show that the supporting substrate should be fully considered in studies aiming at unraveling molecular dopant/TMDC monolayer interactions, as also CT processes may be affected. Therefore, investigating molecular dopant/ML-TMDC interfaces on different types of substrates is crucial for obtaining a comprehensive understanding of the CT processes and the energy levels, which is needed for reliably tuning ML-TMDC electronic properties for device applications.

In this study, we investigate molecular acceptor/ML-TMDC/substrate systems using insulating (sapphire³¹), semi-metallic (highly oriented pyrolytic graphite (HOPG)), and metallic (Au) substrates. With angle-resolved ultraviolet photoelectron

spectroscopy (ARUPS) and X-ray photoelectron spectroscopy (XPS), we monitor the changes of E_F , the sample work function (Φ), and core levels induced by acceptor deposition. According to our observations, we identify three distinct CT mechanisms between the acceptor molecules (1,3,4,5,7,8-hexafluoro-tetracyano-naphthoquinodimethane (F₆TCNNQ)) and ML-TMDC (MoS₂), depending on substrate type. The mechanisms for electron transfer from the (i) MoS₂ gap states to the acceptors (sapphire), (ii) substrate to acceptors with an electric field across the ML-MoS₂ (HOPG), (iii) combined metal/ML-MoS₂ system to acceptors. The difference between (ii) and (iii) is rooted in the different electronic coupling strength between the ML-MoS₂ and the substrates. Consequently, factual doping of MoS₂ proceeds only on the insulating substrates.

Results

Impact of CT on work function and valence electronic levels.

To investigate how CT processes between a TMDC monolayer and the molecular acceptor F₆TCNNQ, which has also been employed as p-type dopant for organic semiconductors, could be influenced by the choice of substrate, ARUPS measurements were performed for MoS₂/sapphire, MoS₂/HOPG, and MoS₂/Au with stepwise deposition of F₆TCNNQ. We note that the MoS₂ monolayers used in this study consist of azimuthally disordered flakes. However, owing to the specific features of the TMDC band structure—related to the high symmetry of the TMDCs—ARUPS spectra feature a high photoemission intensity only along the Γ -K and Γ -M directions of the single-crystal Brillouin zone (BZ), thus the spectra correspond to a linear superposition of the electronic bands along the aforementioned high symmetry directions^{32,33}. We note that, while it was shown that the electrical conductivity of sapphire can increase to about 10^{−9} S/m by creating a high density of defects after annealing to 600 °C and proton bombardment³¹, our experimental conditions ensure the insulating character of sapphire. Particularly, for samples with insufficient MoS₂ monolayer coverage and thus no percolation pathways for CT, we were not able to record any photoemission spectrum due to sample charging (also after sample annealing).

The ARUPS spectra measured in normal emission, as shown in Fig. 1, correspond to the electronic states at the Γ point of the BZ. These Γ point spectra show the highest intensity in the entire BZ, with the top valence band (VB) as an intense and sharp peak, allowing any spectral energy shifts to be accurately resolved. In addition, all spectra in this study exhibit a rigid energy shift upon molecular acceptor deposition, without band distortions (within instrument resolution), indicating that any momentum line cut (1D spectra along energy) provides the same information on energy shifts (exemplified in Supplementary Fig. 1 for the Γ and K points). For clarity, we stress that the global VB maximum is not at the Γ point (VBM _{Γ}), which is only a local maximum point in the band structure, but at the K point (VBM_K). Thus, the K point should be considered for determining the MoS₂ ionization energy (IE), with IE = Φ + VBM_K (with all valence energy levels referenced to E_F)³⁴. VBM _{Γ} , determined by a linear extrapolation of the emission onset toward the background from the spectra in Fig. 1, is at 1.80 eV BE for the pristine MoS₂ films on sapphire and HOPG, and at 1.30 eV BE on Au. In analogy, VBM_K was determined to be at 1.78 eV BE on sapphire, 1.70 eV BE on HOPG, and 1.28 eV BE on Au substrates (see Fig. 2). There is a very small substrate-dependent variation (not more than 0.08 eV) in the energy difference between VBM _{Γ} and VBM_K, which might be related to the presence of defect states of MoS₂ monolayer and/or substrate-specific interactions. Moreover, the MoS₂ monolayer on HOPG might be more homogeneous, leading to the slightly wider energy difference between VBM _{Γ} and VBM_K.

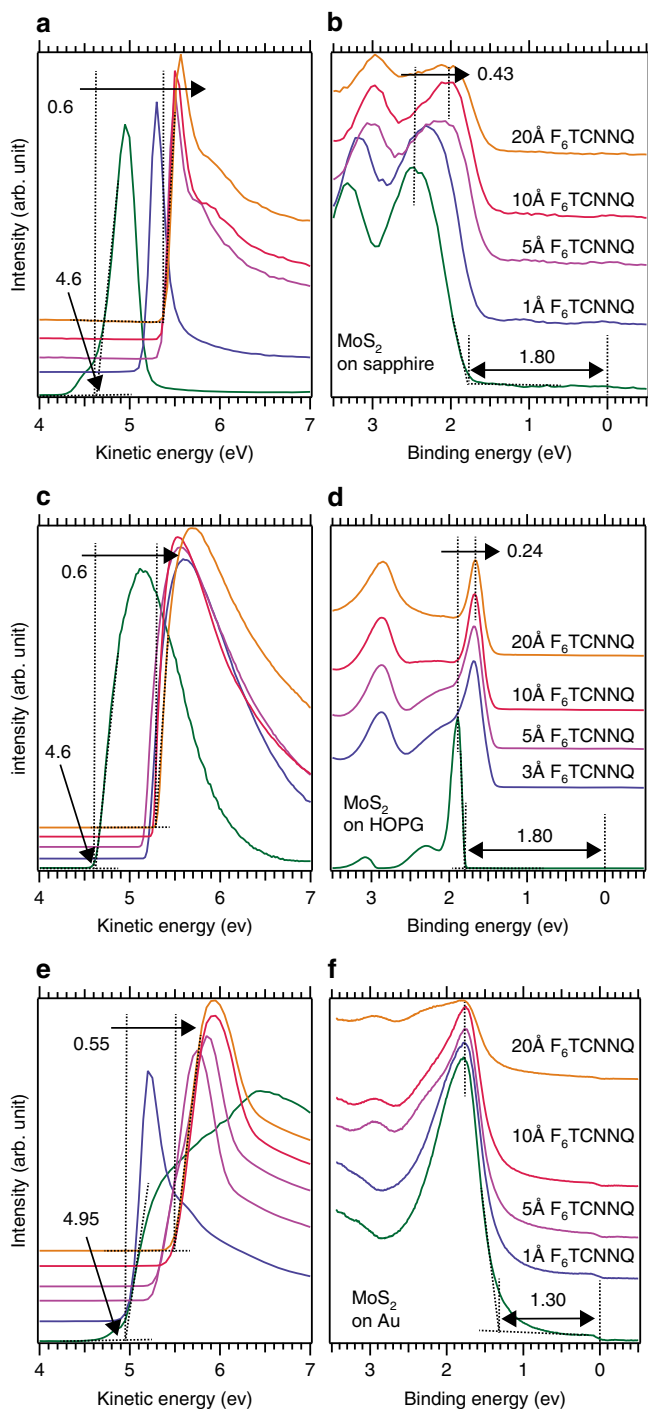


Fig. 1 Angle resolved ultraviolet photoelectron spectra of F_6TCNNQ/MoS_2 /substrate (sapphire, highly oriented pyrolytic graphite (HOPG), and Au) heterostructures. Secondary electron cutoff and valence band (VB) spectra of MoS_2 /sapphire (**a, b**), MoS_2 /HOPG (**c, d**), and MoS_2 /Au (**e, f**) for different F_6TCNNQ coverages. A work function increase of -0.6 eV is observed for all samples after acceptor adsorption. All VB spectra were recorded at the Γ point. The unit of numbers inside the plots is electron volts (eV), which indicate initial sample work function and its change upon F_6TCNNQ deposition (**a, c, e**), and initial valence band onset and its change upon F_6TCNNQ deposition (**b, d, f**)

As seen from Fig. 1a, c, and e, the SECO spectra provide sample Φ values of 4.60 eV for MoS_2 /sapphire, 4.60 eV for MoS_2 /HOPG, and 4.95 eV for MoS_2 /Au. With increasing coverage of F_6TCNNQ , Φ changes ($\Delta\Phi$) are observed, and $\Delta\Phi$ saturates at

approximately $+0.6$ eV at a nominal acceptor layer mass-thickness of 10 Å for all the samples. Apparently, this large $\Delta\Phi$ is related to electron transfer from ML- MoS_2 /substrate to the lowest unoccupied molecular orbital (LUMO) level of F_6TCNNQ , with a possible contribution stemming from orbital polarization. Concomitantly, as shown in Fig. 1b, d, and f, VBM_{Γ} shifts toward lower BE by 0.43 eV for MoS_2 /sapphire and 0.24 eV for MoS_2 /HOPG, while no shift is observed for MoS_2 /Au. Although $\Delta\Phi$ values are the same within 0.05 eV for all the samples, the strongly substrate-dependent VBM_{Γ} shifts already indicate fundamentally different CT mechanisms.

Gap states of the MoS_2 monolayer and F_6TCNNQ anions. To obtain detailed insight into the different CT mechanisms, high-resolution VB spectra of the individual ML- MoS_2 /substrate systems around the K point were measured prior and after deposition of 5 Å F_6TCNNQ , as shown in Fig. 2. In Fig. 2a, a clear photoemission feature is observed just below E_F , i.e., within the technically empty band gap of ML- MoS_2 . We suggest that this feature stems from gap states related to the presence of sulfur vacancies, as predicted by previous studies^{35–37}, and found experimentally for bulk and liquid exfoliated MoS_2 ³⁸. However, investigating the exact origin of these gap state would necessitate extensive additional experiments, which is beyond the scope of the present study.

Most notably, the gap states observed for MoS_2 /sapphire are not present for MoS_2 /HOPG as well as MoS_2 /Au (Fig. 2b, c), although the MoS_2 monolayers transferred to HOPG and Au were synthesized under the same conditions compared to those on sapphire, and underwent the same cleaning procedure in UHV. Thus, the likely reason for the absence of gap states is that the (semi-) metallic substrates (HOPG and Au) withdrew the electrons from the gap states of the monolayer, resulting in now unfilled gap states not observable in an ARUPS experiment.

With nominally 5 Å of F_6TCNNQ adsorbed on ML- MoS_2 /sapphire (Fig. 2a), two features related to the molecules (marked “A” at 0.3 eV BE and “B” at 0.8 eV BE) are observed. As shown in Fig. 2b, these features are also clearly detected for F_6TCNNQ on MoS_2 /HOPG, with essentially the same A/B intensity ratio. According to previous reports, these states can be assigned to anionic F_6TCNNQ (F_6TCNNQ^{-1}), resulting from electron transfer to the molecules^{39,40}. This assignment is further confirmed by density functional theory (DFT) calculations as provided in the Supplementary Note 1. Specifically, these calculations show that upon adding one electron to the LUMO level of an isolated molecule, strong orbital rearrangements occur, which give rise to two gap states that are a combination of (i) the former highest occupied molecular orbital (HOMO) level and the singly filled former LUMO level (peak A), and (ii) the former HOMO and HOMO-1 levels (peak B). In addition, comparison of the spectra obtained with and without 5 Å F_6TCNNQ on MoS_2 /sapphire reveals that the peak positions of the gap states and peak A are too similar to be distinguished. If no CT occurs, the intensity of the gap states (in the chosen momentum interval around K) should be ca. 65% of that observed for the bare ML- MoS_2 because of the attenuation due to the F_6TCNNQ overlayer, as deduced from the attenuation of the Mo 4d valence feature. Thus, peak A would be the sum of the gap states and peak A from F_6TCNNQ^{-1} , if the gap states still existed. However, the relative intensities of peaks A and B for F_6TCNNQ^{-1} on MoS_2 /sapphire and MoS_2 /HOPG are almost identical, though no gap states existed for the pristine MoS_2 /HOPG sample. From this, we infer that the gap states are quenched, i.e., emptied, as a result of the electron transfer from MoS_2 to F_6TCNNQ , when using sapphire as supporting substrate. As for the pristine MoS_2 /HOPG no gap

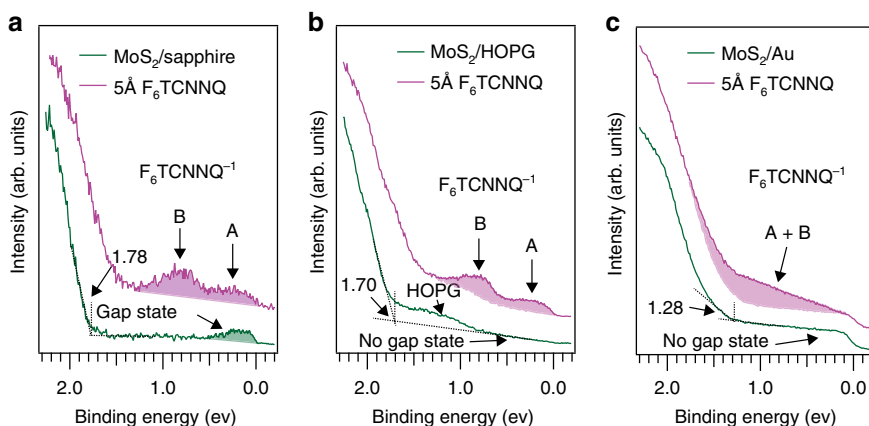


Fig. 2 Energy distribution curves (EDCs) near Fermi level (E_F). EDCs obtained by integration of the corresponding angle-resolved ultraviolet photoelectron spectra around the K point in a narrow interval ($1.08\text{--}1.36 \text{ \AA}^{-1}$), of **a** $\text{MoS}_2/\text{sapphire}$, **b** $\text{MoS}_2/\text{highly oriented pyrolytic graphite (HOPG)}$, and **c** MoS_2/Au with (violet) and without (green) adsorbed F_6TCNNQ . The numbers inside the plots correspond to the MoS_2 valence band onset, given in electron volts (eV)

states are detected, the origin of the electrons transferred to the molecules must therefore be different. In contrast, much broader molecule-induced features are observed for $\text{F}_6\text{TCNNQ}/\text{MoS}_2/\text{Au}$ (Fig. 2c), which yet calls for another CT mechanism as compared to when using sapphire and HOPG substrates. Consequently, three different CT mechanisms are at play for the three studied cases, which are discussed in more detail in the following.

Impact of CT on the individual heterostructure components.

To assess the involvement of the individual components, i.e., ML- MoS_2 versus substrate, in the CT processes, core level spectra of the three ML- $\text{MoS}_2/\text{substrate}$ systems with increasing F_6TCNNQ coverage are analyzed, and displayed in Fig. 3. Note, the F 1s level is related only to F_6TCNNQ molecules and the Mo 3d level to the MoS_2 monolayer. The Al 2p, C 1s, and Au 4f levels are representative of the sapphire, HOPG, and Au, respectively.

First, we attend to the F 1s core level that is indicative of the oxidation state of F_6TCNNQ . As apparent from Fig. 3a, d, and g, the F 1s core levels for 5 \AA F_6TCNNQ on all substrates are observed at 686.7 eV ($\pm 0.05 \text{ eV}$), which dominantly represents $\text{F}_6\text{TCNNQ}^{-1}$ owing to the interfacial CT. With increasing F_6TCNNQ coverage, F 1s levels shift by $0.3\text{--}0.5 \text{ eV}$ toward higher BE, due to an increasing contribution from neutral F_6TCNNQ molecules that become predominant in the multilayer film. Therefore, for all three systems, the F 1s core level spectra consistently confirm the occurrence of electron transfer from the $\text{MoS}_2/\text{substrate}$ system to the acceptor.

Before discussing the details of the Mo 3d and Al 2p core levels, the energy reference in XPS is briefly reiterated. Because of the electrically insulating properties of sapphire, the position of E_F within the band gap of the (grounded) MoS_2 monolayer serves as the energy reference for the XPS measurements. When F_6TCNNQ is adsorbed on top of the MoS_2 monolayer, electrons are transferred from MoS_2 to the F_6TCNNQ molecules, which results in a change in E_F (ΔE_F) in the MoS_2 monolayer (Fig. 1b). Because the ML- MoS_2 is electrically connected to the detector, E_F is re-aligned to 0 eV BE again, resulting in a rigid shift (same value of ΔE_F) for all ML- $\text{MoS}_2/\text{sapphire}$ spectra. For this reason, the Mo 3d and Al 2p core level shifts observed for $\text{MoS}_2/\text{sapphire}$ are due to a change in E_F within the MoS_2 monolayer, and not due to any chemical shifts. For $\text{MoS}_2/\text{sapphire}$ (Fig. 3b), a shift of Mo 3d by up to 0.3 eV toward lower BE is observed, depending on the F_6TCNNQ coverage. As explained above, this is due to the Fermi level shift, as caused by p-doping of the MoS_2 monolayer.

The concomitant shift of the Al 2p core level (sapphire) by the same amount further supports the interpretation of the E_F shift in ML- MoS_2 due to doping by the acceptors.

In contrast, for ML- MoS_2 on HOPG and Au, the energy reference (E_F) is that of the highly conductive (semi-) metallic substrates. In Fig. 3f, the C 1s core level at 284.4 eV can be assigned to the sp^2 carbons of HOPG. Regardless of the F_6TCNNQ coverage, the BE of the HOPG level remains constant, and only decreasing intensity is observed because of the signal attenuation by the F_6TCNNQ overlayer. The same is observed for the Au 4f core level at 84 eV BE in Fig. 3i. Both substrate core level spectra series indicate that the energy reference does not depend on the F_6TCNNQ coverage when conductive substrates are employed.

Remarkably, for ML- MoS_2/HOPG , the Mo 3d core level shifts by 0.25 eV to lower BE upon acceptor deposition, the same as did VBM_T (compare Figs. 1d and 3e). These rigid shifts support the notion of p-doping of MoS_2 monolayer/HOPG. In contrast, for MoS_2/Au , the Mo 3d core levels exhibit no energy shift, as shown in Fig. 3h. This evidences that the interfacial CT did not affect the electronic properties of the MoS_2 monolayer, in full agreement with the constant VBM_T in Fig. 1f. For the three investigated systems, quantitatively different Mo 3d core level shifts are observed, all being consistent with the respective VBM_T shifts in Fig. 1. Since the Mo 3d and S 2p core levels of the MoS_2 shift in parallel (see Supplementary Fig. 2), notable site-specific chemical reactions between the molecular dopant and the monolayer can be ruled out. These findings, in combination with the same $\Delta\Phi$ observed for all three substrate types, further imply three fundamentally different CT mechanisms.

Identification of three CT mechanisms. All experimental findings significantly differ depending on the employed substrate, invoking different CT mechanisms, which seem to be strongly influenced by the interaction between the MoS_2 monolayer and the supporting substrate. Because the heterostructures comprise strong molecular acceptors, a MoS_2 monolayer, and a substrate, two different CT pathways should be considered, namely: (i) a direct CT occurring between the acceptors and the ML- MoS_2 , and (ii) an indirect CT between acceptors and the substrate, possibly involving the MoS_2 monolayer.

We start by testing the direct CT scenario for the three substrates according to the measured energy levels. Considering the reported electron affinity (EA) of F_6TCNNQ (5.6 eV)⁴¹ and the measured IE

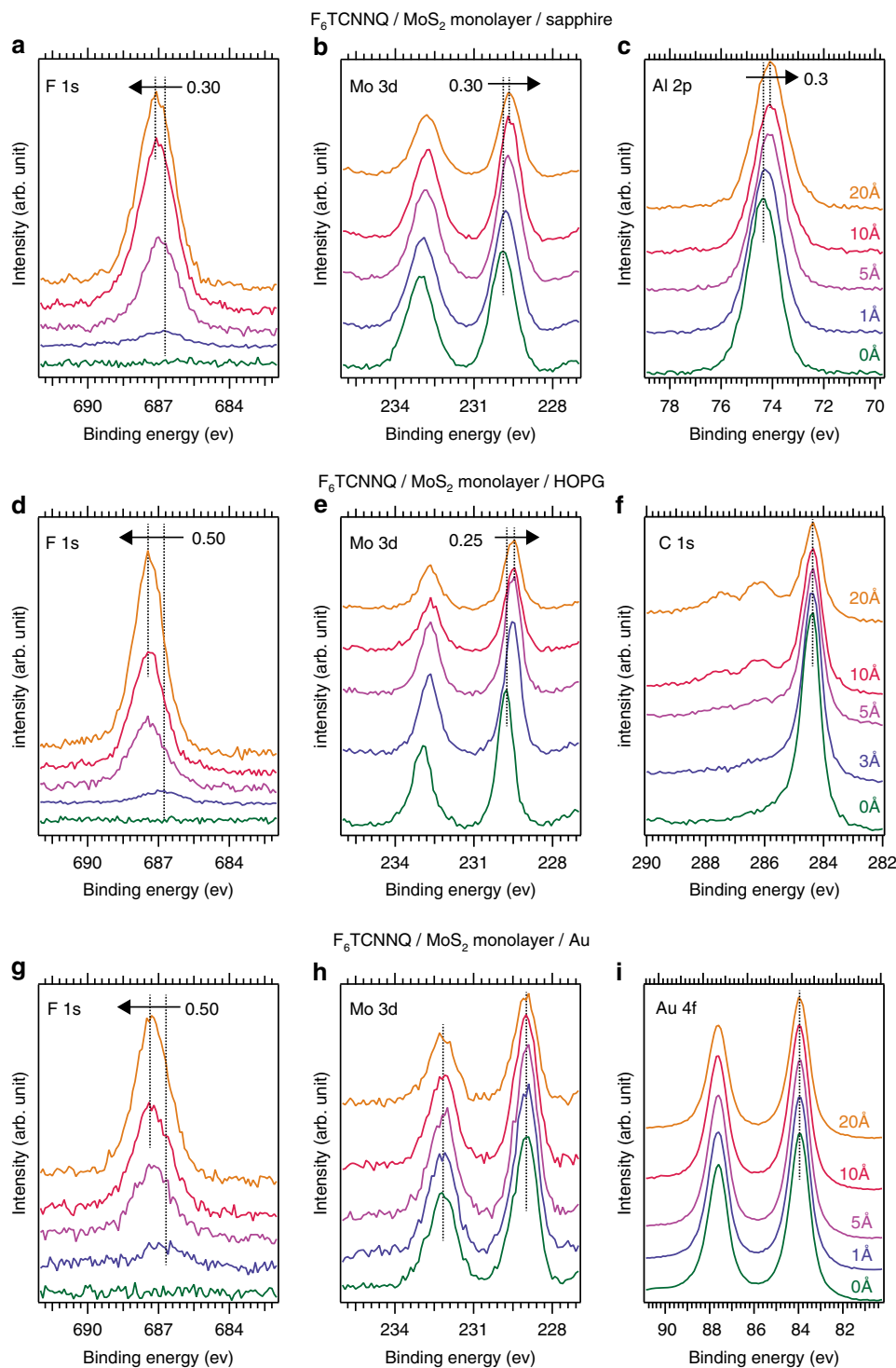


Fig. 3 X-ray photoelectron spectroscopy (XPS) core level spectra. XPS spectra for MoS₂/sapphire (**a–c**), MoS₂/highly oriented pyrolytic graphite (HOPG) (**d–f**), and MoS₂/Au (**g–i**) heterostructures with different F₆TCNNQ coverage, given in Angstrom (Å) in the right handside plots. The numbers inside the plots correspond to the core level shifts, given in electron volts (eV)

of ML-MoS₂, with $IE = \Phi + VBM_K = 4.6 + 1.78 = 6.38$ eV for sapphire, 6.30 eV for HOPG, and 6.23 eV for Au, the possibility of CT from the MoS₂ VB to the F₆TCNNQ LUMO level can be ruled out. Another possible CT pathway is from thermally excited electrons in the MoS₂ global conduction band minimum (CBM_K) to F₆TCNNQ. The EA of ML-MoS₂/substrate is obtained from the determined IE values (see above) and the reported substrate-dependent band gaps ($EA = IE - \text{band gap}$), yielding EA values of 4.27 eV (on sapphire), 4.19 eV (on HOPG), and 4.33 eV (on Au).

The energy difference between the EA of ML-MoS₂ and the EA of F₆TCNNQ supports transfer of thermally excited electrons. In this case, the electron density (n_e) in the conduction band is an important factor. The n_e of ML-MoS₂ is estimated from⁴²

$$n_e = \frac{g_v m_e^* k_B T}{2\pi \hbar^2} \ln \left(1 + e^{(E_F - E_C)/k_B T} \right), \quad (1)$$

where g_v , m_e^* , \hbar , k_B , T , and E_C represent the valley degeneracy factors, the band edge effective mass of electrons, the reduced

Planck constant, the Boltzmann constant, the absolute temperature, and the energy position of the CBM_K , respectively. Using $g_v = 6$, $m_e^* = 0.37m_0$, and $E_C = 0.33 \text{ eV}$, n_e is estimated to be $\sim 10^7 \text{ cm}^{-2}$ (refs. 43,44).

For examining the impact of n_e on eventual CT, we also estimate the density ρ ($e\text{-cm}^{-2}$) of charge transferred into the LUMO levels of F_6TCNNQ molecules adsorbed on ML-MoS₂ by using the measured $\Delta\Phi$ and VBM shift (ΔVBM), according to the Helmholtz equation^{45,46}:

$$\rho = \frac{eD \times \epsilon_{\text{eff}} \epsilon_0}{ed_{\text{eff}}}, \quad (2)$$

where eD , ϵ_0 , ϵ_{eff} , d_{eff} , and e are the interface dipole, the vacuum permittivity, the effective dielectric constant, the effective dipole distance, and the elementary charge, respectively. The eD value can be determined from $eD = \Delta\Phi - \Delta\text{VBM}$, with ΔVBM being the change in VBM binding energy before and after acceptor adsorption. From our data, eD is found to amount to 0.17 eV (sapphire), 0.36 eV (HOPG), and 0.55 eV (Au)^{45,47,48}. With eD thus being in the range of 0.17–0.55 eV and using theoretical values of 4.70 for ϵ_{eff} (corresponding to the average of $\epsilon_{\text{MoS}_2 \text{ ML}} = 6.4$ and $\epsilon_{\text{F}_6\text{TCNNQ}} = 3$) and 3 Å for d_{eff} ^{45,49}, ρ is found to be $\sim 10^{13} \text{ cm}^{-2}$, providing an estimate of the density of the electrons transferred to an F_6TCNNQ monolayer for all samples. Clearly, the estimated density of transferred charge ρ to the F_6TCNNQ exceeds by far (ca. six orders of magnitude) the estimated available electron density in the conduction band. This allows ruling out direct CT from the conduction band as the predominant process in all three cases.

Furthermore, the estimated n_e ($\sim 10^7 \text{ cm}^{-2}$) is small compared to the reported carrier density in MoS₂ monolayers ($\sim 10^{13} \text{ cm}^{-2}$), which necessitates the existence of gap states between the CBM and VBM^{42,50}. Gap states in 2D TMDCs fabricated via chemical vapor deposition (CVD) thus appear as critical factors for the mechanisms of interfacial CT and energy level alignment. Numerous reports have attributed gap states in ML-MoS₂ on insulating substrates, e.g., SiO₂ and sapphire, to S-vacancies owing to their lower formation energy as compared to Mo-vacancies^{35–37,51,52}. Accordingly, gap states have been invoked as key for the energy level alignment at metal/ML-MoS₂ interfaces^{51,53}.

In the present work, for MoS₂/sapphire, a clear gap state is observed near E_F with an IE of 4.6 eV, which is energetically favorable for electron transfer to F_6TCNNQ , and judged from the spectral weight in Fig. 2a it has a sufficient density. This gap state, which is in the present study unique to MoS₂/sapphire, allows direct CT, i.e., from the MoS₂ gap state to the LUMO level of F_6TCNNQ , to occur, as confirmed by the quenching of this state after acceptor adsorption (see Fig. 2a and its discussion above). This is fully in line with the proposition of Wang et al.²².

In contrast, for the ML-MoS₂ on HOPG and Au substrates (Fig. 2b, c), no gap states are observed, which therefore rules out the possibility of direct CT for these two cases. To explain the origin of the transferred charge, the supporting substrate should be considered as an electron reservoir, since Φ_{HOPG} (4.7 eV) and Φ_{Au} (5.3 eV) are both lower than the F_6TCNNQ EA (5.6 eV). Therefore, electron transfer from HOPG and Au to F_6TCNNQ through the MoS₂ monolayer is plausible. For ML-MoS₂/HOPG, electrons accumulate in the F_6TCNNQ layer and their image charges in HOPG, which leads to a high electric field between HOPG and F_6TCNNQ . The concomitant electrostatic potential drop across the ML-MoS₂, sandwiched between acceptor layer and substrate, shifts the energy levels of the MoS₂, which appears to become p-type doped via this indirect CT. A similar indirect CT process has been suggested for the $\text{C}_{60}\text{F}_{48}/\text{WSe}_2/\text{HOPG}$ interface, and ultra-thin organic heterojunctions on metal substrates^{26,54}.

Finally, for ML-MoS₂/Au, the absence of energy level shifts (MoS₂ valence and core levels) upon acceptor deposition is caused by a strong electronic coupling of the TMDC and Au, as orbital hybridization between ML-MoS₂ and Au has been previously reported⁵⁵. In this case, the electrons are transferred from the hybridized ML-MoS₂/Au system, which acts as an electron reservoir, to F_6TCNNQ .

Discussion

Figure 4 summarizes simplified schematics of the three proposed CT mechanisms and the corresponding energy level diagrams for the investigated systems. On general grounds, owing to the low dimensionality of 2D TMDCs, the CT between 2D TMDCs and dopant molecules (acceptors and donors) is strongly influenced by the properties of the surrounding medium, i.e., the supporting substrate. Depending on the insulating, semi-metallic, and metallic properties of the substrate, as well as the coupling strength between the 2D TMDC and the substrate, three different cases can be classified:

(1) Insulating substrate: Direct CT occurs between the 2D TMDC valence levels (if energetically allowed, not the case for the materials investigated here) or gap states (observed in this work) to the LUMO level of the molecular acceptor, resulting in p-type doping of the 2D TMDC, as illustrated in Fig. 4a and d. Note that in the present case, the ML-MoS₂ starts out highly n-type (due to the gap states) and doping by F_6TCNNQ depletes the gap states, rendering the monolayer less n-type by 0.4 eV. For molecular donors and n-type doping, an analogous mechanism can proceed.

(2) Weakly coupled (semi-) metallic substrate: Indirect CT occurs from the substrate to the dopant molecule, through the MoS₂ monolayer as shown in Fig. 4b, e. The charges accumulated in the molecular layer and the substrate lead to a high electric field across the 2D TMDC, resulting in an ostensible doping of the TMDC layer.

(3) Strongly coupled metallic substrate: CT occurs from the 2D TMDC-metal hybridized frontier level to the LUMO level of the molecular acceptor, as shown in Fig. 4c and f. Because of the strong coupling, the energy levels of the 2D TMDC are pinned to those of the metal substrate and no doping of the 2D TMDC layer proceeds despite substantial CT.

We emphasize that in all three cases above, the sample Φ increased upon F_6TCNNQ deposition by virtually the same amount. Consequently, a change of the TMDC/substrate Φ induced by molecular acceptors/donors (or other dopants deposited atop the TMDC) cannot be used as a reliable indicator for doping of the semiconductor. Likewise, a shift of E_F , as observed here for the HOPG substrate, can result from an electric field drop across the ML-TMDC, induced by the charges in the molecular layer and the substrate; this situation is reminiscent of a parallel plate capacitor where the TMDC is the dielectric between the two plates. Only if the substrate can be ruled out as source of charges for the dopants, factual doping of the TMDC occurs, which is crucially important when aiming to study the fundamental behavior of ML-TMDCs as a function of carrier density. Moreover, with the knowledge of the three different CT mechanisms and how they can be implemented, a wide variety of possibilities to fine-tune the electronic properties of ML-TMDCs in device heterostructures becomes available.

Methods

Sample preparation. MoS₂ monolayers were grown on sapphire via CVD and transferred onto an HOPG or Au substrate. The monolayers consist of interconnected individual flakes, thus featuring high overall surface coverage and percolation paths for charge carriers, as exemplarily shown by optical micrographs in Supplementary Fig. 3. Prior to the ARUPS and XPS measurements, all MoS₂ monolayer samples were annealed overnight at 300–350 °C in situ in an ultrahigh vacuum (UHV) preparation chamber (10^{-9} mbar) to remove carbon

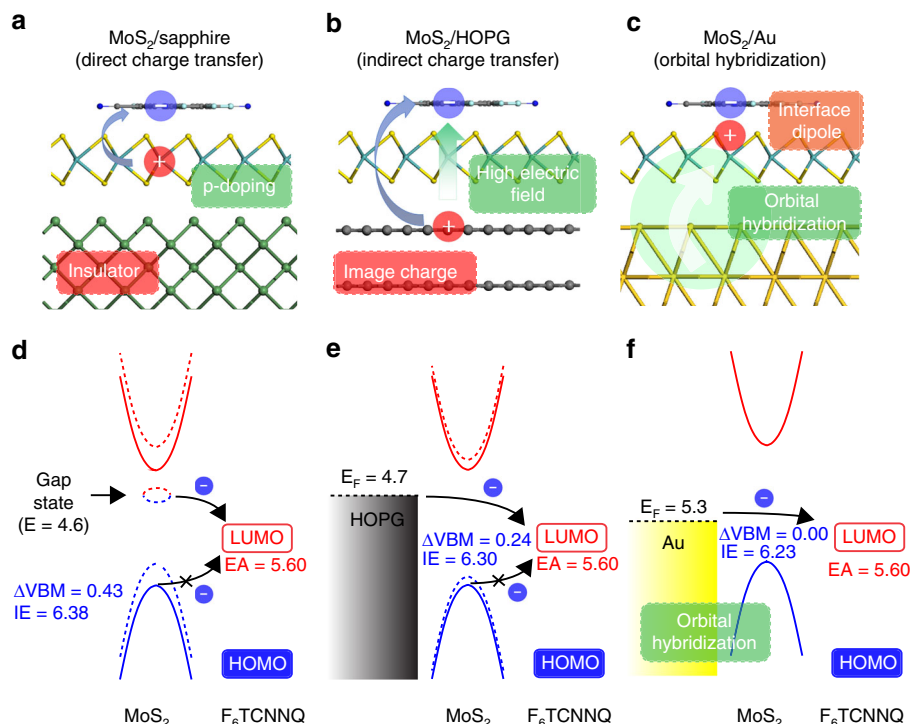


Fig. 4 Schematics of the mechanisms of charge transfer (CT) between MoS₂/substrate and F₆TCNNQ. **a** Direct CT (MoS₂/sapphire, 2D transition metal dichalcogenides (TMDC)/insulator), **b** indirect CT (MoS₂/highly oriented pyrolytic graphite (HOPG), 2D TMDC/weakly interacting conductor), and **c** orbital hybridization with CT (MoS₂/Au, 2D TMDC/strongly interacting conductor). Corresponding energy level diagrams for **d** F₆TCNNQ/ML-MoS₂/sapphire, **e** F₆TCNNQ/ML-MoS₂/HOPG, and **f** F₆TCNNQ/ML-MoS₂/Au. The solid and dashed lines indicate the levels before and after F₆TCNNQ adsorption, respectively. The blue and red lines denote the occupied and unoccupied states, respectively. All the values are given in electron volts (eV)

contaminations and residual poly(methyl methacrylate) involved during the transfer process. F₆TCNNQ (Novaled) was deposited in the preparation chamber by sublimation from a resistively heated quartz crucible, and the nominal mass-thickness was determined via quartz crystal microbalance measurements.

Photoemission measurements. ARUPS and XPS spectra were obtained using a hemispherical electron analyzer (SCIENTA DA30L) using He I_α (21.22 eV) and Mg K_α (1253.6 eV) as excitation sources, respectively. The energy resolution of ARUPS and XPS of 0.13 eV and 0.75 eV was determined by the width of the Fermi edge of a clean Au sample and the full-width at half-maximum (FWHM) of the Au 4f core level, respectively. For all the shown ARUPS spectra, the contribution from the He I_β satellite was removed. The work function (Φ) values were determined from the secondary electron cutoff (SECO) spectra, measured with −10 V sample bias. For the sapphire substrate, proper MoS₂ monolayer electrical grounding was established by contacting all sample edges with metal clips (connected to the metal sample holder), to prevent charging during the photoemission measurement. For HOPG and Au substrates, the MoS₂ monolayer was connected to the ground through the conductive substrates.

Data availability

The authors declare that the data supporting the findings of this study are available within the paper and its supplementary information file, and source data are also available from the corresponding author upon reasonable request.

Received: 30 July 2019 Accepted: 20 August 2019

Published online: 13 September 2019

References

- Wang, Q. H., Kalantar-Zadeh, K., Kis, A., Coleman, J. N. & Strano, M. S. Electronics and optoelectronics of two-dimensional transition metal dichalcogenides. *Nat. Nanotechnol.* **7**, 699–712 (2012).
- Chhowalla, M. et al. The chemistry of two-dimensional layered transition metal dichalcogenide nanosheets. *Nat. Chem.* **5**, 263–275 (2013).
- McDonnell, S. J. & Wallace, R. M. Atomically-thin layered films for device applications based upon 2D TMDC materials. *Thin Solid Films* **616**, 482–501 (2016).
- Radisavljevic, B. et al. Single-layer MoS₂ transistors. *Nat. Nanotechnol.* **6**, 147–150 (2011).
- Wang, H. et al. Integrated circuits based on bilayer MoS₂ transistors. *Nano Lett.* **12**, 4674–4680 (2012).
- He, Q. et al. Fabrication of flexible MoS₂ thin-film transistor arrays for practical gas-sensing applications. *Small* **8**, 2994–2999 (2012).
- Late, D. J. et al. Sensing behavior of atomically thin-layered MoS₂ transistors. *ACS Nano* **7**, 4879–4891 (2013).
- Sarkar, D. et al. MoS₂ field-effect transistor for next-generation label-free biosensors. *ACS Nano* **8**, 3992–4003 (2014).
- Buscema, M. et al. Large and tunable photothermoelectric effect in single-layer MoS₂. *Nano Lett.* **13**, 358–363 (2013).
- Yin, Z. et al. Single-layer MoS₂ phototransistors. *ACS Nano* **6**, 74–80 (2012).
- Bernardi, M., Palummo, M. & Grossman, J. C. Extraordinary sunlight absorption and one nanometer thick photovoltaics using two-dimensional monolayer materials. *Nano Lett.* **13**, 3664–3670 (2013).
- Zhao, W. et al. Evolution of electronic structure in atomically thin sheets of WS₂ and WSe₂. *ACS Nano* **7**, 791–797 (2013).
- Tongay, S. et al. Broad-range modulation of light emission in two-dimensional semiconductors by molecular physisorption gating. *Nano Lett.* **13**, 2831–2836 (2013).
- Kylänpää, I. & Komsa, H.-P. Binding energies of exciton complexes in transition metal dichalcogenide monolayers and effect of dielectric environment. *Phys. Rev. B* **92**, 205418 (2015).
- Cheng, Y. C., Zhu, Z. Y., Mi, W. B., Guo, Z. B. & Schwingschlögl, U. Prediction of two-dimensional diluted magnetic semiconductors: doped monolayer MoS₂ systems. *Phys. Rev. B* **87**, 100401 (2013).
- Duan, X. et al. Lateral epitaxial growth of two-dimensional layered semiconductor heterojunctions. *Nat. Nanotechnol.* **9**, 1024–1030 (2014).
- Ma, D. et al. The adsorption of CO and NO on the MoS₂ monolayer doped with Au, Pt, Pd, or Ni: a first-principles study. *Appl. Surf. Sci.* **383**, 98–105 (2016).
- Rastogi, P., Kumar, S., Bhowmick, S., Agarwal, A. & Chauhan, Y. S. Doping strategies for monolayer MoS₂ via surface adsorption: a systematic study. *J. Phys. Chem. C* **118**, 30309–30314 (2014).

19. Dolui, K., Rungger, I., Das Pemmaraju, C. & Sanvito, S. Possible doping strategies for MoS₂ monolayers: an *ab initio* study. *Phys. Rev. B* **88**, 075420 (2013).
20. Du, Y., Liu, H., Neal, A. T., Si, M. & Ye, P. D. Molecular doping of multilayer MoS₂ field-effect transistors: reduction in sheet and contact resistances. *IEEE Electron Device Lett.* **34**, 1328–1330 (2013).
21. Tarasov, A. et al. Controlled doping of large-area trilayer MoS₂ with molecular reductants and oxidants. *Adv. Mater.* **27**, 1175–1181 (2015).
22. Wang, J. et al. Charge transfer within the F4TCNQ-MoS₂ van der Waals interface: toward electrical properties tuning and gas sensing application. *Adv. Funct. Mater.* **28**, 1806244 (2018).
23. Nevola, D. et al. Rigid valence band shift due to molecular surface counter-doping of MoS₂. *Surf. Sci.* **679**, 254–258 (2019).
24. Zhang, S. et al. Controllable, wide-ranging n-doping and p-doping of monolayer group 6 transition-metal disulfides and diselenides. *Adv. Mater.* **30**, 1802991 (2018).
25. Wang, Y. et al. Doping of monolayer transition-metal dichalcogenides via physisorption of aromatic solvent molecules. *J. Phys. Chem. Lett.* **10**, 540–547 (2019).
26. Song, Z. et al. Electronic properties of a 1D intrinsic/p-doped heterojunction in a 2D transition metal dichalcogenide semiconductor. *ACS Nano* **11**, 9128–9135 (2017).
27. Katoch, J. et al. Giant spin-splitting and gap renormalization driven by trions in single-layer WS₂/h-BN heterostructures. *Nat. Phys.* **14**, 355–359 (2018).
28. Raja, A. et al. Coulomb engineering of the bandgap and excitons in two-dimensional materials. *Nat. Commun.* **8**, 15251 (2017).
29. Drüppel, M., Deilmann, T., Krüger, P. & Rohlfing, M. Diversity of trion states and substrate effects in the optical properties of an MoS₂ monolayer. *Nat. Commun.* **8**, 2117 (2017).
30. Kim, C. et al. Fermi Level Pinning at Electrical Metal Contacts of Monolayer Molybdenum Dichalcogenides. *ACS Nano* **11**, 1588–1596 (2017).
31. Pells, G. P. & Sowden, B. C. The electrical conductivity of sapphire irradiated at 550–700 °C with an applied electric field of 1 kV/cm. *J. Nucl. Mater.* **223**, 174–179 (1995).
32. Zhou, S. Y. et al. Coexistence of sharp quasiparticle dispersions and disorder features in graphite. *Phys. Rev. B* **71**, 161403 (2005).
33. Park, S. et al. Electronic band dispersion determination in azimuthally disordered transition-metal dichalcogenide monolayers. *Commun. Phys.* **2**, 68 (2019).
34. Ramasubramanian, A. Large excitonic effects in monolayers of molybdenum and tungsten dichalcogenides. *Phys. Rev. B* **86**, 115409 (2012).
35. Guo, Y., Liu, D. & Robertson, J. Chalcogen vacancies in monolayer transition metal dichalcogenides and Fermi level pinning at contacts. *Appl. Phys. Lett.* **106**, 173106 (2015).
36. Liu, D., Guo, Y., Fang, L. & Robertson, J. Sulfur vacancies in monolayer MoS₂ and its electrical contacts. *Appl. Phys. Lett.* **103**, 183113 (2013).
37. Wang, D., Li, X.-B., Han, D., Tian, W. Q. & Sun, H.-B. Engineering two-dimensional electronics by semiconductor defects. *Nano Today* **16**, 30–45 (2017).
38. Donarelli, M., Bisti, F., Perrozzi, F. & Ottaviano, L. Tunable sulfur desorption in exfoliated MoS₂ by means of thermal annealing in ultra-high vacuum. *Chem. Phys. Lett.* **588**, 198–202 (2013).
39. Timpel, M. et al. Electrode Work Function Engineering with Phosphonic Acid Monolayers and Molecular Acceptors: Charge Redistribution Mechanisms. *Adv. Funct. Mater.* **28**, 1704438 (2018).
40. Braun, S. & Salaneck, W. R. Fermi level pinning at interfaces with tetrafluorotetracyanoquinodimethane (F₄-TCNQ): The role of integer charge transfer states. *Chem. Phys. Lett.* **438**, 259–262 (2007).
41. Zhang, F. & Kahn, A. Investigation of the High Electron Affinity Molecular Dopant F₆-TCNNQ for Hole-Transport Materials. *Adv. Funct. Mater.* **28**, 1703780 (2018).
42. Ma, N. & Jena, D. Carrier statistics and quantum capacitance effects on mobility extraction in two-dimensional crystal semiconductor field-effect transistors. *2D Mater.* **2**, 015003 (2015).
43. Cheiwchanmanngij, T. & Lambrecht, W. R. L. Quasiparticle band structure calculation of monolayer, bilayer, and bulk MoS₂. *Phys. Rev. B* **85**, 205302 (2012).
44. Peelaers, H. & Van de Walle, C. G. Effects of strain on band structure and effective masses in MoS₂. *Phys. Rev. B* **86**, 241401 (2012).
45. Wang, C. et al. Charge transfer at the PTCDA/black phosphorus interface. *J. Phys. Chem. C* **121**, 18084–18094 (2017).
46. Anger, F. et al. Interface dipole and growth mode of partially and fully fluorinated rubrene on Au(111) and Ag(111). *J. Phys. Chem. C* **119**, 6769–6776 (2015).
47. Ashcroft, N. W. & Mermin, N. D. *Solid State Physics*. (Elsevier, New York, 1976).
48. Oehzelt, M., Koch, N. & Heimel, G. Organic semiconductor density of states controls the energy level alignment at electrode interfaces. *Nat. Commun.* **5**, 4174 (2014).
49. Laturia, A., Van de Put, M. L. & Vandenberghe, W. G. Dielectric properties of hexagonal boron nitride and transition metal dichalcogenides: from monolayer to bulk. *npj 2D Mater. Appl.* **2**, 6 (2018).
50. Kim, S. et al. High-mobility and low-power thin-film transistors based on multilayer MoS₂ crystals. *Nat. Commun.* **3**, 1011 (2012).
51. McDonnell, S., Addou, R., Buie, C., Wallace, R. M. & Hinkle, C. L. Defect-dominated doping and contact resistance in MoS₂. *ACS Nano* **8**, 2880–2888 (2014).
52. Zhou, W. et al. Intrinsic structural defects in monolayer molybdenum disulfide. *Nano Lett.* **13**, 2615–2622 (2013).
53. Bampoulis, P. et al. Defect dominated charge transport and fermi level pinning in MoS₂/metal contacts. *ACS Appl. Mater. Interfaces* **9**, 19278–19286 (2017).
54. Amsalem, P. et al. Role of charge transfer, dipole-dipole interactions, and electrostatics in Fermi-level pinning at a molecular heterojunction on a metal surface. *Phys. Rev. B* **87**, 035440 (2013).
55. Bruix, A. et al. Single-layer MoS₂ on Au(111): band gap renormalization and substrate interaction. *Phys. Rev. B* **93**, 165422 (2016).

Acknowledgements

This work was funded by the Deutsche Forschungsgemeinschaft (DFG) - Projektnummer 182087777 - SFB 951. S.P. acknowledges support by the Alexander von Humboldt-Stiftung. V.T. acknowledges the support from KAUST Solar Center Seed fund and under User Proposals (#4420 and #5067) at the Molecular Foundry, Lawrence Berkeley National Lab, supported by the Office of Basic Energy Sciences, of the U.S. Department of Energy under Contract No. DE-AC02-05CH11231. This work was supported by the KIST Institutional Program (Project No. 2E29850) and the National Research Foundation (NRF) of Korea under Grant 2018M3D1A1058793, funded by the Korean Government. Part of Fig. 4 was created with the software VESTA (Momma, K. and Izumi, F. VESTA 3 for three-dimensional visualization of crystal, volumetric and morphology data. *J. Appl. Crystallogr.* **44**, 1272–1276 (2011)).

Author contributions

S.P., T.S., and P.A. prepared the manuscript, measured the samples using ARUPS and XPS, and analyzed all data, under the supervision of N.K. X.X., B.W., and P.A. revised the manuscript. A.A., A.H., L.L., and V.C.T. prepared the 2D TMDCs samples. All authors commented on the manuscript.

Additional information

Supplementary information accompanies this paper at <https://doi.org/10.1038/s42005-019-0212-y>.

Competing interests: The authors declare no competing interests.

Reprints and permission information is available online at <http://npj.nature.com/reprintsandpermissions/>

Publisher's note Springer Nature remains neutral with regard to jurisdictional claims in published maps and institutional affiliations.



Open Access This article is licensed under a Creative Commons Attribution 4.0 International License, which permits use, sharing, adaptation, distribution and reproduction in any medium or format, as long as you give appropriate credit to the original author(s) and the source, provide a link to the Creative Commons license, and indicate if changes were made. The images or other third party material in this article are included in the article's Creative Commons license, unless indicated otherwise in a credit line to the material. If material is not included in the article's Creative Commons license and your intended use is not permitted by statutory regulation or exceeds the permitted use, you will need to obtain permission directly from the copyright holder. To view a copy of this license, visit <http://creativecommons.org/licenses/by/4.0/>.

© The Author(s) 2019